

## Development of patient-specific biomechanical models for predicting large breast deformation

This content has been downloaded from IOPscience. Please scroll down to see the full text.

2012 Phys. Med. Biol. 57 455

(<http://iopscience.iop.org/0031-9155/57/2/455>)

View [the table of contents for this issue](#), or go to the [journal homepage](#) for more

Download details:

IP Address: 202.118.72.32

This content was downloaded on 08/08/2014 at 01:51

Please note that [terms and conditions apply](#).

## Development of patient-specific biomechanical models for predicting large breast deformation

Lianghao Han<sup>1,4</sup>, John H Hipwell<sup>1</sup>, Christine Tanner<sup>2</sup>, Zeike Taylor<sup>3</sup>,  
Thomy Mertzani<sup>1</sup>, Jorge Cardoso<sup>1</sup>, Sebastien Ourselin<sup>1</sup>  
and David J Hawkes<sup>1</sup>

<sup>1</sup> Centre for Medical Image Computing, Department of Medical Physics and Bioengineering, University College London, Gower Street, London, UK

<sup>2</sup> Computer Vision Laboratory, ETH Zürich, 8092 Zürich, Switzerland

<sup>3</sup> Department of Mechanical Engineering, University of Sheffield, Sheffield, UK

E-mail: [l.han@ucl.ac.uk](mailto:l.han@ucl.ac.uk), [j.hipwell@ucl.ac.uk](mailto:j.hipwell@ucl.ac.uk), [t.mertzani@ucl.ac.uk](mailto:t.mertzani@ucl.ac.uk),  
[manuel.cardoso@ucl.ac.uk](mailto:manuel.cardoso@ucl.ac.uk), [s.ourselin@ucl.ac.uk](mailto:s.ourselin@ucl.ac.uk), [d.hawkes@ucl.ac.uk](mailto:d.hawkes@ucl.ac.uk),  
[tanner@vision.ee.ethz.ch](mailto:tanner@vision.ee.ethz.ch) and [z.a.taylor@sheffield.ac.uk](mailto:z.a.taylor@sheffield.ac.uk)

Received 29 August 2011, in final form 31 October 2011

Published 15 December 2011

Online at [stacks.iop.org/PMB/57/455](http://stacks.iop.org/PMB/57/455)

### Abstract

Physically realistic simulations for large breast deformation are of great interest for many medical applications such as cancer diagnosis, image registration, surgical planning and image-guided surgery. To support fast, large deformation simulations of breasts in clinical settings, we proposed a patient-specific biomechanical modelling framework for breasts, based on an open-source graphics processing unit-based, explicit, dynamic, nonlinear finite element (FE) solver. A semi-automatic segmentation method for tissue classification, integrated with a fully automated FE mesh generation approach, was implemented for quick patient-specific FE model generation. To solve the difficulty in determining material parameters of soft tissues *in vivo* for FE simulations, a novel method for breast modelling, with a simultaneous material model parameter optimization for soft tissues *in vivo*, was also proposed. The optimized deformation prediction was obtained through iteratively updating material model parameters to maximize the image similarity between the FE-predicted MR image and the experimentally acquired MR image of a breast. The proposed method was validated and tested by simulating and analysing breast deformation experiments under plate compression. Its prediction accuracy was evaluated by calculating landmark displacement errors. The results showed that both the heterogeneity and the anisotropy of soft tissues were essential in predicting large breast deformations under plate compression.

<sup>4</sup> Author to whom any correspondence should be addressed.

As a generalized method, the proposed process can be used for fast deformation analyses of soft tissues in medical image analyses and surgical simulations.

(Some figures may appear in colour only in the online journal)

## 1. Introduction

Physically realistic modelling of breasts has great potentials in medical applications such as cancer diagnosis, image registration, surgical planning and image-guided surgery. A common requirement for these applications is to provide the estimation of large deformation. Biomechanical models using finite element (FE) methods have been employed for this aim in assisting breast cancer diagnosis (Ruiter *et al* 2002), MR image-guided biopsy (Azar *et al* 2001), image registration (Han *et al* 2011, Rajagopal *et al* 2010, Ruiter *et al* 2006) and surgical simulations (del Palomar *et al* 2008, Lapuebla-Ferri *et al* 2011). Typically two kinds of breast deformations were investigated: compression deformation by plates and gravity loading deformation. Plate compression simulations were used to build the spatial correspondence between the 2D projection and the 3D volume of the breast in multimodality image registration (Chung *et al* 2008, Kellner *et al* 2007, Ruiter *et al* 2006), or between undeformed and deformed 3D volumes in MR image-guided biopsy (Azar *et al* 2001). Deformation simulations of breasts under gravity were used to estimate the breast shape change with the patient's position change in breast surgical planning and image-guided surgery (Carter *et al* 2006, Han *et al* 2011, Ruiter *et al* 2006).

In previous studies, breast tissues were simulated with linear elastic or nonlinear hyperelastic models and a wide range of material properties for breast tissues were used, mainly from *ex vivo* experimental data. Some studies on breast compression showed that the deformation of breasts depended very weakly on the material model and mechanical properties of breast tissues (Azar *et al* 2001, Tanner *et al* 2006). This was due to the fact that in these studies the plate compression was modelled with the so-called displacement loading, i.e. by applying displacement constraints to the surface of a breast. To investigate the real effects of material properties and material models on breast deformation in a physically based biomechanical model, the interaction between the compression plate and the breast tissues should be explicitly modelled, e.g. with a contact model.

Both the accuracy and the computation time of patient-specific modelling are important in clinical applications. Although commercial FE packages (e.g. ABAQUS, ANSYS, LS-DYNA and MSC/MARC) are very powerful tools for large deformation simulations, longer computational time will limit their applications in clinical settings. To perform real-time computations on large soft tissue deformation, we developed a nonlinear FE solver, implemented on graphics processing units (GPUs) for parallel execution (Taylor *et al* 2008, 2009). More recently, a frictionless contact model was implemented to facilitate interaction simulations such as the contact between compression plates and breast tissues during x-ray mammogram (Tzu-Ching *et al* 2010), and the sliding between tissues and the chest wall (Han *et al* 2011).

The original contributions presented in this paper include the following: (1) to support fast, large deformation simulation of breasts for clinical applications, we propose a patient-specific biomechanical modelling framework based on a fast, open-source, nonlinear FE solver implemented in our group; (2) to solve the difficulty in determining the material parameters of soft tissues *in vivo* for FE simulations, we develop a novel material parameter

**Table 1.** Breast volume, maximum compression and tissue types in the compression experiment.

Patient	Breast volume (cm <sup>3</sup> )	Maximum compression (%)	Tissue types
Case 1	1364	31.9	fat, fibroglandular tissue, muscle, tumour
Case 2	865	38.9	fat, fibroglandular tissue, muscle
Case 3	464	40.0	fat, fibroglandular tissue, muscle
Case 4	1064	50.4	fat, fibroglandular tissue, muscle
Case 5	716	19.4	fat, fibroglandular tissue, muscle

optimization procedure for breast tissues *in vivo*; and (3) we describe our implementation of a semi-automatic process for quick generation of patient-specific FE models from MR volume images, which includes tissue classification, surface extraction, FE volumetric mesh generation and material parameter assignment. Using breast compression experiments and MR breast images before and after compression, specifically acquired for plate compression studies, we have evaluated the prediction accuracy of the proposed method and investigated the effect of material models on the deformation prediction.

## 2. Materials and methods

### 2.1. MR image data of breasts

To present and evaluate the method for patient-specific biomechanical modelling of breasts subject to large deformation, we simulated and analysed a group of five breast compression experiments. In the compression experiments, a specially designed experimental rig (Tanner *et al* 2011), consisting of a support structure, a fixed plate and a movable plate, was used to compress breasts, similar to the compression process occurring during x-ray mammogram or MR image-guided biopsy. MR image data were acquired for both uncompressed and compressed breasts in prone position. Uncompressed MR images were acquired when the breast of a patient was placed between the two parallel plates without any applied force from the movable plate, while compressed MR images were acquired after the movable plate was moved manually towards the fixed plate as much as the patient could comfortably tolerate. The MR images had a voxel size of  $1.0 \times 1.0 \times 2.5 \text{ mm}^3$ . As listed in table 1, the maximum compressions on breasts were within the range of 19–50% of initial breast thickness. For each case, 17 landmarks, including 12 internal landmarks, 4 fiducial markers on the breast surface and the nipple, were selected in the uncompressed MR image, and their corresponding positions in the compressed MR image were also identified.

### 2.2. Patient-specific FE model of breasts

To generate a patient-specific FE model from magnetic resonance images (MRI), we follow four steps. These are as follows: (1) tissue classification/segmentation, (2) tissue surface reconstruction, (3) FE volumetric mesh generation and (4) FE model construction. Both the tissue segmentation and the FE mesh generation often require manual intervention. In this study, a semi-automatic segmentation approach and a fully automated mesh generation method were implemented in order to minimize manual intervention and reduce the time for FE model construction.

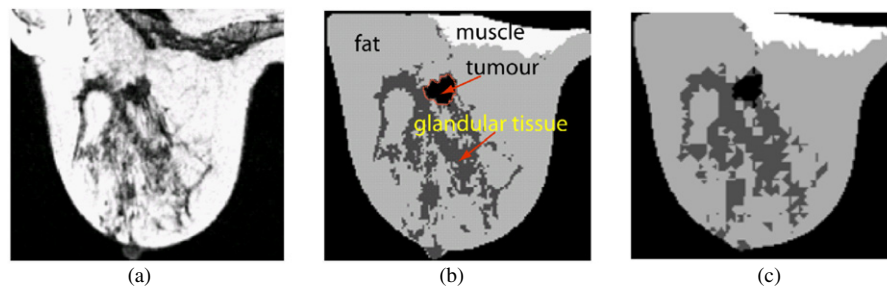


**Figure 1.** Breast MR segmentation and material assignment: (a) original, axial MR slice, (b) after segmentation and (c) after tissue assignment to FE elements.

**2.2.1. Tissue classification.** A female breast is essentially composed of glandular lobules, milk ducts, fat and Cooper's ligaments, surrounded by muscle and skin (Netter 2010). Cooper's ligaments, running from the pectoral fascia through and around breast tissues to the dermis of the skin, are connective tissues to support the breast. Figure 1(a) shows an example of MR breast images. In this image, fibroglandular tissues (dark gray), fatty tissues (light gray), skin (light gray), tumour (dark) and muscle (dark gray) are visible in the MR image, while Cooper's ligaments are invisible. Considering that the skin has little influence on breast deformation in compression experiments (Azar 2001, Ruiter *et al* 2006, Tanner *et al* 2006), we treat skin and fat as a single material (labelled fat for convenience). All MR volume images were therefore segmented into fat, fibroglandular tissue, pectoral muscle and tumour (if present). The pectoral muscle was first segmented from the rest of the breast volume, manually, using an interactive tool in ANALYZE ([www.analyzeirect.com](http://www.analyzeirect.com)). Once the pectoral muscle was segmented, an automated method, integrating an intensity model, a spatial regularization scheme and bias field inhomogeneity correction, was used to segment fat and fibroglandular tissue from the pre-contrast breast MR image (Mertzanidou *et al* 2010, Cardoso *et al* 2011). The method consists of an expectation-maximization algorithm with Markov random field regularization, which has been implemented as an open-source program called NiftySeg (<http://niftyseg.sourceforge.net>). Compared to thresholding methods, this method gives a more detailed description of the fibroglandular tissue by calculating a probability of each tissue type being present in each voxel. This is the *partial volume effect* in which a voxel may represent more than one kind of tissues. We then assume that a voxel has a specified tissue type if its probability value is more than 0.5 for this tissue type. Tumour was also segmented manually using ANALYZE. Thus, the tissue type was fully determined for every voxel in an MR image. Figure 1 shows the tissue structure of a breast in the 2D image slice before and after segmentation.

**2.2.2. Surface reconstruction of breast tissues.** To generate the volume mesh of a breast, the surface of each tissue type was first determined from segmented MR images using a marching cube algorithm (Lorenson and Cline 1987). The tissue segmentation eliminated surface ambiguities in the marching cube process. The surface generation process was very fast due to direct triangulation from a look-up-table of properties for the marching cube routine. To obtain the computational efficiency for FE analyses, smoothing and decimation processes were employed. Figure 2(a) shows the surfaces of four different tissues extracted from the segmented MR image shown in figure 1(b). The surface reconstruction process was completed in less than 10 s.

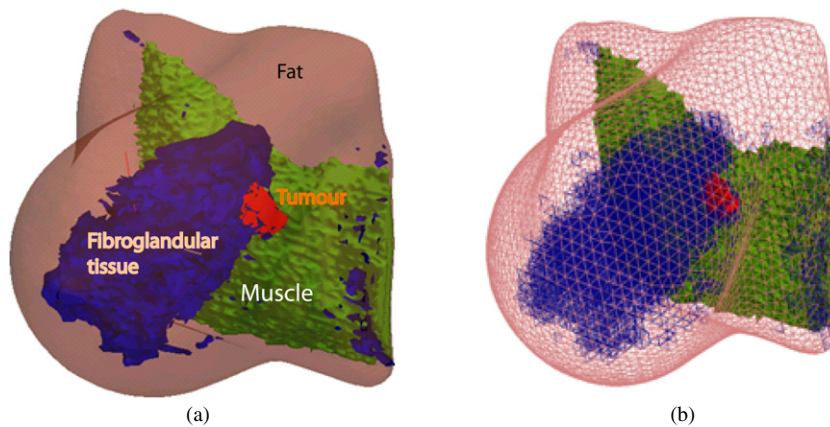


**Figure 2.** Example tissue model: (a) 3D surfaces of four tissue types and (b) 3D FE volumetric mesh representing these tissue types.

**2.2.3. FE mesh generation.** Mesh generation is often the most time consuming component of FE analyses. It is still a challenging task to mesh arbitrary, multiple material domains for good-quality meshes. Although commercial software, such as Hypermesh<sup>TM</sup>, ANSYS/ICEM CFD and Simpleware<sup>TM</sup>, can be used for multi-domain meshing, these require time-consuming manual intervention and repair (Wittek *et al* 2010). To facilitate the automation of FE meshing, we used a single-domain tetrahedral meshing algorithm to automatically generate a patient-specific, 3D volumetric mesh based on the tissue surfaces extracted from segmented MR images. The automatic process of tetrahedral meshing consisted of two steps: a coarse meshing process followed by a refining process. A coarse mesh was generated from the whole surface of a breast with Tetgen (<http://tetgen.berlios.de/>), an open-source mesh generator for 3D tetrahedron meshing. To generate an FE mesh accurately representing the geometry of each tissue type, the coarse mesh was refined by using the sparse points on the surfaces of each tissue type as additional insert points in Tetgen. Figure 2(b) illustrates a 3D FE mesh generated from the surfaces of the whole breast and from the surfaces of four tissue types shown in figure 2(a). For this example, the whole breast was meshed into 29 307 nodes and 161 997 four-node tetrahedral elements. The mesh quality was checked by ABAQUS/CAE using three default element failure criteria: shape factor ( $<0.001$ ), face corner angle ( $<5$  or  $>150$ ) and aspect ratio ( $>10$ ). The shape factor is defined as the ratio of element volume and optimal element volume, where optimal element volume is the volume of an equilateral tetrahedron with the same circumradius as that of the element (the circumradius is the radius of the sphere passing through the four vertices of the tetrahedron). The face corner angle is the angle between the two edges of a surface in a tetrahedral element. The aspect ratio is the ratio between the longest and the shortest edge of an element. Breast tissues are highly incompressible; therefore, a four-node linear tetrahedral element type with an improved average nodal pressure (ANP) formulation (Joldes *et al* 2009) was employed in order to prevent over-stiffening and volumetric locking in the tetrahedral elements.

**2.2.4. Tissue type assignment for FE mesh.** The tissue type was automatically assigned to each 3D element in the FE mesh based on tissue classification results in the MR image. First, we found all the voxels within an element by determining whether the centre of a voxel was inside or outside of the element; then we counted the number of the voxels belonging to each

tissue type from these voxels, based on tissue classification. The tissue type corresponding to the highest number of voxels was assigned to this element. Repeating the process above, we assigned each element with a unique tissue type. For the case shown in figure 2(b), 134 314 elements were assigned to fat, 11 250 elements to fibroglandular tissue, 16 334 elements to muscle and 99 elements to tumour. The final tissue distribution within the FE mesh was shown in figure 1(c). Compared to the tissue distribution in the segmented MR, as shown in figure 1(b), the tissue assignment to the FE mesh demonstrates a good approximation to the tissue representation. Obviously, the finer the mesh, the more precise the assignment of tissue type will be. However, a finer mesh also means more computation time in the FE analyses. There is a balance, therefore, between the accuracy of the tissue type representation in an FE model and the computational time in the FE analyses.

*2.2.5. Constitutive model for breast tissues.* Like most biological soft tissues, breast tissues exhibit nonlinear, anisotropic and time (rate)-dependent responses under large deformation (Han *et al* 2002). The large recoverable deformation of soft tissues is often modelled via hyperelastic material models. The time (rate) dependence could be considered by augmenting time-dependent material parameters with the hyperelastic formulation, forming visco-hyperelastic constitutive models for soft tissues (Taylor *et al* 2009). Many hyperelastic models (such as neo-Hookean, Mooney–Rivlin, Ogden, Arruda–Boyce models, polynomial, etc) have been developed for soft tissues. The constitutive model of a hyperelastic material is defined by a total stress versus total strain relationship derived from a strain energy function, which can be expressed as

$$W = W(\mathbf{C}), \quad (1)$$

where  $\mathbf{C} = \mathbf{X}^T \mathbf{X}$  is the right Cauchy–Green deformation tensor, and  $\mathbf{X} = \partial {}^t x / \partial {}^0 x$  is the deformation gradient tensor related to the current point,  ${}^t x$ , and the reference configuration,  ${}^0 x$ , of a material particle. The stress–strain relationship is derived from (1) as

$$\mathbf{S} = 2\partial W / \partial \mathbf{C}, \quad (2)$$

where  $\mathbf{S}$  is the second Piola–Kirchhoff stress tensor.

If a material is isotropic, the strain energy function can be written as

$$W = W(I_1, I_2, I_3), \quad (3)$$

where  $I_1$ ,  $I_2$  and  $I_3$ , are the three principal invariants of  $\mathbf{C}$ , which are given by

$$I_1 = \text{tr } \mathbf{C}, \quad I_2 = \frac{1}{2}[(\text{tr } \mathbf{C})^2 - \text{tr}(\mathbf{C}^2)], \quad I_3 = \det \mathbf{C} = J^2. \quad (4)$$

For an incompressible material,  $I_3 \equiv 1$ .

Due to the presence of Cooper’s ligaments and connective tissues, breast tissues are anisotropic and could be considered as fibre-reinforced materials. The simplest representation for their anisotropy is transversely isotropic, in which the material is reinforced by a family of fibres and has one preferred direction (i.e. the fibre direction), but the mechanical response along the directions orthogonal to these preferred directions is isotropic. Consequently, an independent invariant directly related to the fibre stretch,  $I_4$ , could be introduced to the strain energy function. The strain energy is written as (Taylor *et al* 2009)

$$W = W(I_1, I_2, I_3, I_4), \quad (5)$$

where  $I_4 = \mathbf{A} \cdot \bar{\mathbf{C}} \mathbf{A}$  is the pseudo-invariant of  $\bar{\mathbf{C}} = J^{-\frac{2}{3}} \mathbf{C}$  and  $\mathbf{A}$  is the direction vector of the fibres and can be defined as

$$\mathbf{A} = \sin \gamma \cos \alpha \mathbf{e}_1 + \sin \gamma \sin \alpha \mathbf{e}_2 + \cos \alpha \mathbf{e}_3 \quad (6)$$

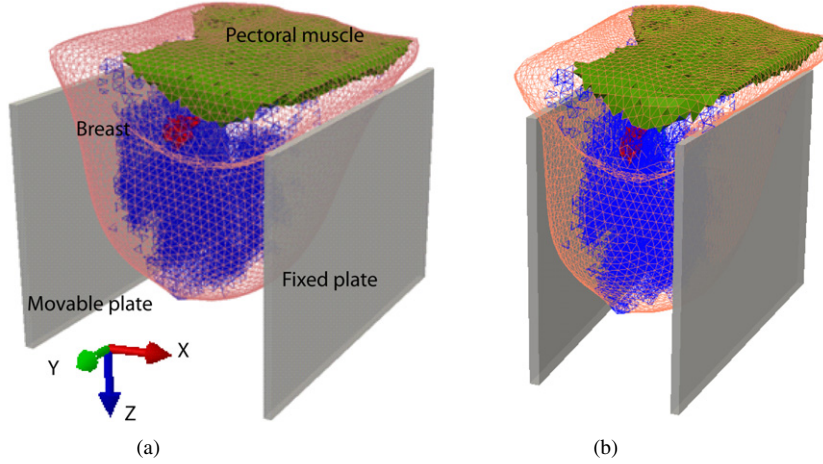


**Figure 3.** FE models for breast deformation analysis: (a) before compression and (b) after compression.

in a rectangular Cartesian coordinate system, where the unit vectors  $\{\mathbf{e}_1, \mathbf{e}_2, \mathbf{e}_3\}$  co-directional with the  $x$ ,  $y$  and  $z$  axes are referred to as  $\mathbf{e}_1 = \begin{bmatrix} 1 \\ 0 \\ 0 \end{bmatrix}$ ,  $\mathbf{e}_2 = \begin{bmatrix} 0 \\ 1 \\ 0 \end{bmatrix}$  and  $\mathbf{e}_3 = \begin{bmatrix} 0 \\ 0 \\ 1 \end{bmatrix}$ , and  $\gamma \in [0, \frac{\pi}{2}]$  represents the angle between  $\mathbf{A}$  and  $\mathbf{e}_3$ , and  $\alpha \in [0, \pi]$  shows the angle between  $\mathbf{A}$  and  $\mathbf{e}_1$ . For the material reinforced by a family of fibres aligned in a specific direction, the strain energy function can be decomposed into an isotropic component and a transversely isotropic component as

$$W = W_{\text{iso}}(I_1, I_2, I_3) + W_{\text{trans}}(I_4). \quad (7)$$

For the sake of simplicity, we chose the neo-Hookean (NH) strain energy function. Then, (7) is rewritten as

$$W_{\text{iso}}(I_1, I_2, I_3) = \frac{\mu}{2}(I_1 - 3) + \frac{k}{2}(J - 1)^2, \quad W_{\text{trans}}(I_4) = \frac{\eta}{2}(I_4 - 1)^2, \quad (8)$$

where  $\mu$  is the initial small strain shear modulus,  $k$  is the bulk modulus and  $\eta$  defines a measure of the strength of fibre reinforcement. Equation (8) forms the simplest anisotropic hyperelastic model. In the model,  $\mu$  and  $k$  can be determined from the other two elastic parameters, initial Young's modulus  $E$  and Poisson's ratio  $\nu$ , through the relationships of  $\mu = E/(2(1 + \nu))$  and  $k = E/(3(1 - 2\nu))$ . If the preferred direction of a tissue can be pre-determined, e.g. if it is much stronger in the  $z$  direction, then  $\mathbf{A} = [0, 0, 1]$ . Thus, only three parameters,  $(E, \nu, \eta)$ , are required to completely define this anisotropic model.

**2.2.6. Loading and boundary conditions.** Unlike previous studies where displacement boundary constraints were applied on the surface nodes of a breast model, to simulate the plate compression (Ruiter *et al* 2006, Tanner *et al* 2006, 2011), the interaction between tissues and plate was modelled with a contact model in this study. Figure 3(a) represents an FE model for breast compression simulations. As shown in figure 3(a), the movable plate will move towards the fixed plate to compress the breast by applying a positive displacement in the  $x$ -direction (i.e. from the outer side of the breast towards the centre of the chest). Two contact pairs were defined, movable plate versus breast tissue and fixed plate versus breast

tissues. The compression plates were considered as rigid bodies and the breast tissues were defined as deformable bodies. The interaction between the breast and compression plates can be considered as either a frictional contact problem (Chung *et al* 2008, Tzu-Ching *et al* 2010) or a frictionless contact problem (Azar *et al* 2002, Pathmanathan 2006, Rajagopal *et al* 2010, Ruiter *et al* 2006). When a frictional contact was simulated, an arbitrary friction coefficient was always assumed (Chung *et al* 2008, Tzu-Ching *et al* 2010) due to the lack of information about friction. To the authors' knowledge, there is no research report on the systematic, experimental or numerical studies of the effect of friction between the compression plate and the skin on the prediction accuracy of breast deformation. However, an experimental observation on the MR breast images of three patients (Azar *et al* 2002) showed that a sliding effect existed between the compression plate and the skin. Therefore, in this study, we assumed that the contact between the compression plates and breast tissues was frictionless like previous studies on plate compression (Azar *et al* 2002, Pathmanathan 2006, Rajagopal *et al* 2010, Ruiter *et al* 2006). The positions and motions of the compression plates were determined based on the surfaces of the compressed breast and the positions of the MR visible fiducial markers attached on the compression plates. All the surface nodes of the pectoral muscle attached to the chest wall were constrained in the  $z$ -direction (i.e. anterior–posterior direction). To prevent rigid body displacements of the whole breast, a surface node of the pectoral muscle nearest to one rib was constrained in the  $y$ -direction as well. Figure 3(b) shows a deformed FE mesh after compression.

### 2.3. Dynamic explicit FE method for large deformation analyses of soft tissue

The breast deformation was previously considered as a static or quasi-static problem, and was analysed using static implicit FE methods (Azar *et al* 2001, Pathmanathan *et al* 2008, Tanner *et al* 2006) or dynamic explicit FE methods (Han *et al* 2010, Tzu-Ching *et al* 2010). In static implicit FE methods, nonlinear equations are solved iteratively. In dynamic explicit methods, partial difference equations are solved by using small time increments, without iterations and without requiring the assembly of tangent stiffness matrices. Although dynamic explicit methods are developed for transient dynamic analyses, they are also suitable for quasi-static processes when inertial forces are kept at negligible levels. The dynamic explicit method is specially favoured for nonlinear contact analyses due to its simplification for the treatment of contact (ABAQUS 2010).

For a dynamic FE analysis, the motion equation of the discretized system is written as (Bathe 1996)

$$\mathbf{M}\ddot{\mathbf{u}} + \mathbf{D}\dot{\mathbf{u}} + \mathbf{K}(\mathbf{u})\mathbf{u} = \mathbf{R}, \quad (9)$$

where  $\mathbf{u}$ ,  $\dot{\mathbf{u}}$  and  $\ddot{\mathbf{u}}$  are the displacement, velocity and acceleration vectors of the FE assemblage;  $\mathbf{M}$  is the constant mass matrix,  $\mathbf{D}$  is the constant damping matrix,  $\mathbf{K}(\mathbf{u})$  is the stiffness matrix which is a function of  $\mathbf{u}$ , and  $\mathbf{R}$  is the vector of externally applied loads. The three terms on the left of (9) represent inertia forces, damping forces and internal forces, respectively. Either explicit (e.g. the central difference operator) or implicit (e.g. the Newmark and backward Euler operators) time integration schemes may be used to solve (9). Implicit schemes calculate dynamic quantities at current time based not only on values at previous time, but also on these same quantities at current time. Therefore, nonlinear equations must be solved and iterations are required. Explicit schemes, as used in ABAQUS/Explicit and LS-DYNA, calculate dynamic quantities at the current time based on available values at previous time. The central difference method is the most commonly used explicit operator for stress analyses. In this study, we used

the explicit central difference integration rule to obtain the acceleration and velocity at time  $t$  as

$${}^t\ddot{\mathbf{u}} = \frac{1}{\Delta t^2} ({}^{t-\Delta t}\mathbf{u} - 2{}^t\mathbf{u} + {}^{t+\Delta t}\mathbf{u}) \quad (10)$$

and

$${}^t\dot{\mathbf{u}} = \frac{1}{\Delta t} (-{}^{t-\Delta t}\mathbf{u} + {}^{t+\Delta t}\mathbf{u}), \quad (11)$$

where the superscript  $t$  refers to the time step.

The displacement solution for time  $t + \Delta t$  is obtained by considering (9) at time  $t$ , i.e.

$$\mathbf{M}{}^t\ddot{\mathbf{u}} + \mathbf{D}{}^t\dot{\mathbf{u}} + {}^t\mathbf{K}{}^t\mathbf{u} = {}^t\mathbf{R}. \quad (12)$$

Substituting (10) and (11) into (12), we obtain

$$\left( \frac{1}{\Delta t^2}\mathbf{M} + \frac{1}{2\Delta t}\mathbf{D} \right) {}^{t+\Delta t}\mathbf{u} = {}^t\mathbf{R} - {}^t\mathbf{K}{}^t\mathbf{u} + \frac{2}{\Delta t^2}\mathbf{M}{}^t\mathbf{u} - \left( \frac{1}{\Delta t^2}\mathbf{M} - \frac{1}{2\Delta t}\mathbf{D} \right) {}^{t-\Delta t}\mathbf{u} \quad (13)$$

from which the displacement at time  $t + \Delta t$ ,  ${}^{t+\Delta t}\mathbf{u}$ , is solved. Note that the internal force term in (13) can be calculated by summing the contributions of each element,  ${}^t\mathbf{K}{}^t\mathbf{u} = {}^t\mathbf{F} = \sum_e {}^t\tilde{\mathbf{F}}^{(e)}$ , where  ${}^t\tilde{\mathbf{F}}^{(e)}$  is the nodal force in element  $e$  at time  $t$ .  ${}^t\tilde{\mathbf{F}}^{(e)}$  may be computed from

$${}^t\tilde{\mathbf{F}}^{(e)} = \int_{V^{(e)}} {}^t\mathbf{B}^T {}^t\mathbf{S} dV, \quad (14)$$

where  ${}^t\mathbf{B}$  is the strain-displacement matrix,  ${}^t\mathbf{S}$  is the second Piola–Kirchhoff stress tensor and  $V^{(e)}$  is the volume of element  $e$ . For the transversely isotropic hyperelastic model,  ${}^t\mathbf{S}$  can be obtained from (2) and (8).

The mass matrix,  $\mathbf{M}$ , could be described as a diagonal lumped matrix, which is one of the important features making the explicit method efficient and practical. If we employ mass-proportional damping (a special case of Rayleigh damping),  $\mathbf{D} = \alpha\mathbf{M}$  is also diagonal, where  $\alpha$  is a constant. Thus, the  $i$ th displacement component of each node is obtained using

$${}^{t+\Delta t}u_i = \frac{{}^tR_i - {}^tF_i + \frac{2m_{ii}}{\Delta t^2}u_i + \left( \frac{\alpha m_{ii}}{2\Delta t} - \frac{m_{ii}}{\Delta t^2} \right) {}^{t-\Delta t}u_i}{\frac{\alpha m_{ii}}{2\Delta t} + \frac{m_{ii}}{\Delta t^2}}, \quad (15)$$

where  ${}^tR_i$  and  ${}^tF_i$  denote the  $i$ th components of the vectors  ${}^t\mathbf{R}$  and  ${}^t\mathbf{F}$ , respectively,  $m_{ii}$  is the  $i$ th diagonal element of the mass matrix, and it is assumed that  $m_{ii} > 0$ . The solution of  ${}^{t+\Delta t}u_i$  is based on only previous time steps, with no iteration, matrix inversion or matrix factorization. Equation (15) shows that the use of diagonal element mass matrices is the key to improving computational efficiency without factorizing a matrix in order to solve the system of nonlinear equations in (13). Additionally, because there is no requirement to assemble the global stiffness matrix, the solution can essentially be carried out on the element level and relatively little high-speed storage is required. Using this approach, systems of equations at very large order could be solved effectively in parallel mode. In contrast to implicit methods, which are unconditionally stable and can have a large time step, explicit methods are conditionally stable and generally require a relatively small time step. The time step,  $\Delta t$ , should be smaller than a critical value,  $\Delta t_{cr}$ , which can be estimated from the mass and stiffness properties of the complete element assemblage (Bathe 1996). Generally, a smaller time step is required for stiffer tissues. The initial conditions and the loading rate are chosen such that inertial effects are negligible.

The dynamic explicit FE solution procedure above was implemented on the GPUs as an open-source FE solver, called NiftySim (<http://niftysim.sourceforge.net/>). In the developed GPU-based dynamic explicit nonlinear FE solver, both geometric and material nonlinearity can be handled. Three element types are available: eight-node linear hexahedron

element with reduced integration, four-node linear tetrahedron element and four-node linear tetrahedral element with an improved ANP formulation for nearly incompressible materials or incompressible materials (Bonet and Burton 1998, Joldes *et al* 2009). Six nonlinear material constitutive models were implemented, including NH hyperelastic, Arruda–Boyce hyperelastic, polynomial hyperelastic, transversely isotropic hyperelastic, NH visco-hyperelastic and transversely isotropic visco-hyperelastic. More recently, we implemented a kinematic-type contact algorithm (Hallquist 2005) for modelling the interaction between a deformable object and a rigid object (e.g. between breast tissues and the rigid compression plate used in x-ray mammography). In this algorithm, a deformable slave surface and a rigid master surface are defined, and the slave nodes found to have penetrated the master surface are relocated to the closest point on the latter during the simulations, approximating a frictionless interface. Arbitrary sliding of a node over the contact surface is allowed.

#### 2.4. Breast compression analysis with simultaneous material parameter optimization

Breast morphology varies with changing physiological conditions and age. It is also highly variable across individuals (Van Houten *et al* 2003). The measured material property parameters were also different under different constraints and loading conditions. To date, most of the experimental work on biomechanical properties of breast tissues has been confined to *ex vivo* tissue samples (Samani and Plewes 2004, Samani *et al* 2007) or restricted to small strain studies (Krouskop *et al* 1998). These measured data are not suitable for patient-specific *in vivo* modelling.

In this study, rather than arbitrarily choosing *ex vivo* data or using pre-optimized material model parameters (Tanner *et al* 2006), we modelled the patient-specific breast deformation under plate compression using a simultaneous material parameter optimization process. Figure 4 presents a flowchart for patient-specific modelling of breasts, which can be described by the following six steps.

- Step 1.* Create the FE model of a breast from its original undeformed MR image following the procedure described in section 2.2, and initialize the material parameters of breast tissues using *ex vivo* data reported in the literature.
- Step 2.* Calculate the deformation field using the GPU-based explicit FE solver introduced in section 2.3 as a solver.
- Step 3.* Generate an FE-predicted deformed MR image by applying the calculated deformation field from step 2 to the original undeformed MR image, through interpolation over elements using element shape functions.
- Step 4.* Calculate the image similarity (e.g. normalized mutual information (NMI), cross correlation) between the FE-predicted deformed MR image and the original deformed MR breast image.
- Step 5.* Check whether the image similarity measure has been maximized or the maximum iteration number has been reached. If both are not satisfied, update the material parameters of tissues based on a global optimization algorithm (e.g. simulated annealing, SA, or genetic algorithm), then go to step 2; or else go to step 6.
- Step 6.* Output the best deformation estimation for the breast.

In the deformation analyses, the best estimation of breast deformation was found by solving a constrained optimization, i.e. by maximizing the image similarity between the predicted MR image of a breast and its original deformed MR image. The image similarity was measured with NMI (Studholme *et al* 1999), defined as

$$\text{NMI}(A, B) = \frac{H(A) + H(B)}{H(A, B)}, \quad (16)$$

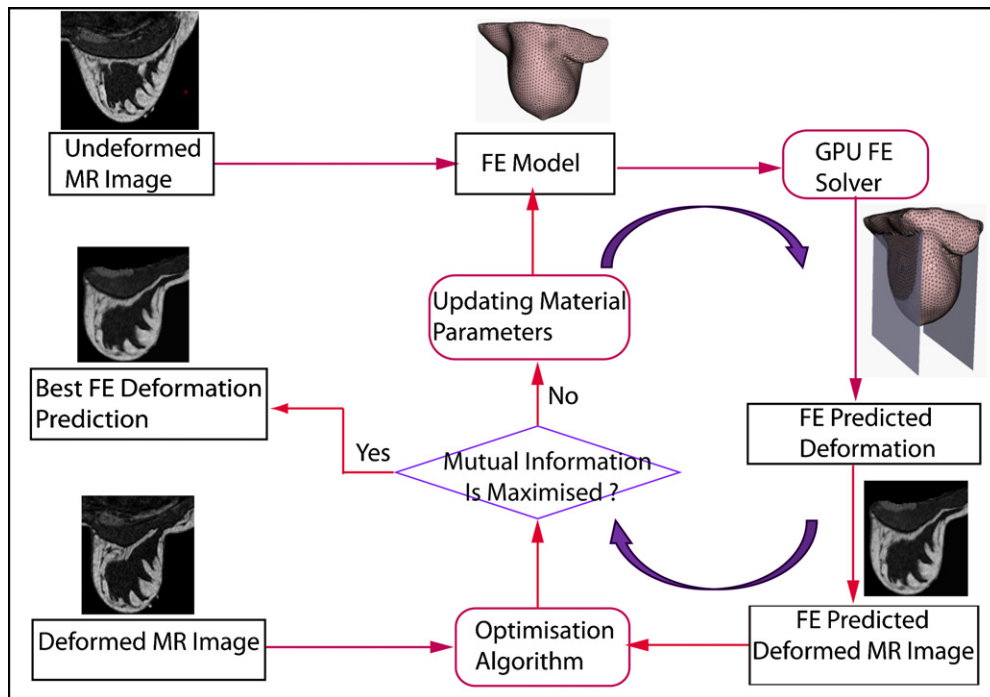


**Figure 4.** A diagram illustrating the patient-specific deformation simulation procedure with simultaneous material parameter optimization.

where  $H(A)$  was the Shannon entropy of the experimentally measured original MR image,  $H(B)$  denoted the entropy of the FE-predicted MR image and  $H(A, B)$  was the entropy of the joint distribution of the measured MR image and the FE-predicted image. The objective function was defined as

$$\arg \min - \text{NMI}(p) \quad \text{subject to} \quad lb < p < ub, \quad (17)$$

where  $p$  was the material parameter vector with the lower bound constraint  $lb$  and the upper bound constraint  $ub$ . NMI is a function of  $p$ , defined as  $(E, \nu, \eta)$  for the transversely isotropic NH hyperelastic model. A hybrid simulated annealing algorithm was chosen for the global optimization. The global search was performed using the MATLAB simulated annealing function, *simulannealbnd*, to find parameter values near the optimum; then with these parameter values as initial values, the local search was performed by calling the MATLAB constrained nonlinear optimization function, *fmincon*. Since a number of iterations are involved, it is very time consuming to use a commercial FE package such as ABAQUS or ANSYS as an FE solver, as this approach would typically require several hours CPU execution time for each 3D FE simulation. However, the GPU-based, dynamic explicit FE solver (Han *et al* 2010, Taylor *et al* 2008) is well suited for this application, because of its high-speed execution.

### 3. Result

We first evaluated the performance of our GPU-based dynamic explicit FE solver for contact modelling. Then, the proposed method was used to analyse the breast deformation under plate

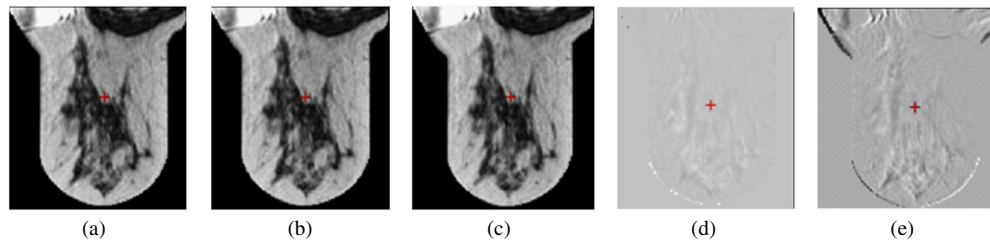


**Figure 5.** Comparison of 2D slice images in the  $X$ - $Z$  plane ( $y = 0$ ) through simulated MR compression volumes obtained with three different solvers: (a) ABAQUS/Standard, (b) ABAQUS/Explicit and (c) NiftySim. The difference images are shown in (d) for the difference between ABAQUS/Standard and ABAQUS/Explicit and (e) for the difference between ABAQUS/Explicit and NiftySim.

compression for the five cases described in section 2.1. All the analyses were performed on a personal computer (Intel dual-core 3.4 GHz, 4 GB, windows 7, 32 bit operation system). The GPU-speedup was supported with an NVIDIA GeForce GTX 285 graphics card with 1 GB memory.

### 3.1. Evaluation for FE solver

The developed GPU-based dynamic explicit FE solver has been evaluated in previous studies (Han *et al* 2010, Taylor *et al* 2008, 2009). In this study, we evaluated the new implementation of a frictionless contact algorithm for breast compression analyses. Since the plate compression process is a slow loading process, we considered the breast compression as a quasi-static process. In the simulations, the kinetic energy was monitored to ensure that the ratio of kinetic energy to internal energy was less than 5%, that is, the dynamic effect could be neglected (Han *et al* 2010, ABAQUS 2010). The FE model for case 1, shown in figure 3, was used as a numerical example for the FE solver evaluation. We assumed that the breast consisted of one homogeneous and isotropic material. An isotropic NH material model with initial Young's modulus in the undeformed state equal to 10 kPa, a Poisson's ratio of 0.49 and mass density of  $1000 \text{ kg m}^{-3}$  was employed. The geometric nonlinearity was considered due to large strain. To evaluate the proposed algorithm, simulation results obtained from our dynamic explicit FE solver, NiftySim, were compared with those calculated with commercial FE solvers, ABAQUS/Standard, a static implicit solver and ABAQUS/Explicit, a dynamic explicit FE solver. As an explicit FE solver, ABAQUS/Explicit can handle much larger deformation than ABAQUS/Standard, without requiring remeshing. For facilitating the comparison, the maximum compression in this numerical example was set to 25% of the maximum thickness of the breast between the two plates. This is the maximum compression that the solution with ABAQUS/Standard can achieve before requiring remeshing, a difficult and time-consuming task. Figure 5 shows 2D slice images from the calculated MR volume images for a compressed breast with the three FE solvers, NiftySim, ABAQUS/Standard and ABAQUS/Explicit. All three calculated images of the compressed breast, as shown in figures 5(a)–(c), cannot be distinguished from each other visually. To find how different two images are, the difference images are obtained, as shown in figures 5(d) and (e). Figure 5(d) is the difference image between the ABAQUS/standard calculation and the ABAQUS/Explicit calculation, which has a maximum displacement difference of 0.5 mm. Figure 5(e) is the difference image between the ABAQUS/Explicit calculation and the NiftySim calculation, which has a maximum

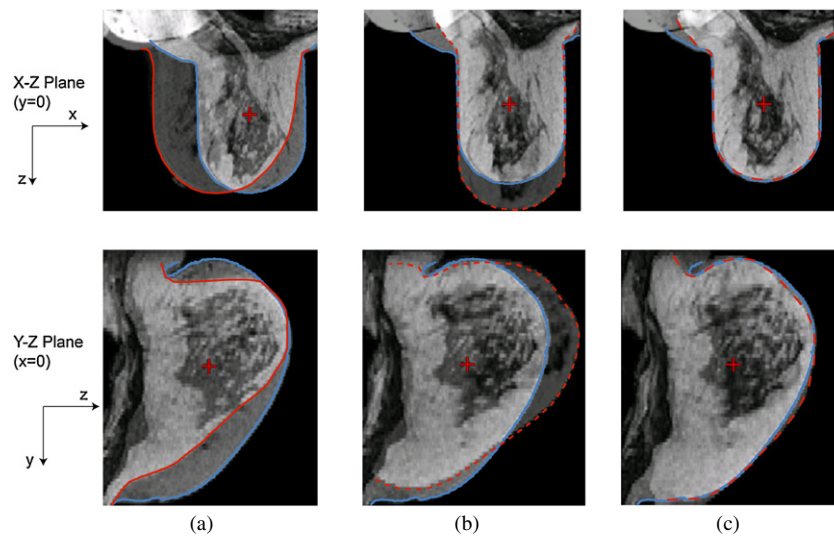


**Figure 6.** Comparison of breast shapes in simulated MR images: (a) the original deformed image superimposed with the original undeformed image, (b) the original deformed image superimposed with the deformed image estimated with the isotropic NH hyperelastic model and (c) the original deformed image superimposed with the deformed image estimated with the transversely isotropic NH hyperelastic model.

displacement difference of 1.2 mm within the region between the two compression plates. The small difference of calculated displacements between NiftySim and ABAQUS/Explicit shows that NiftySim can provide essentially the same accuracy for deformation prediction as ABAQUS/Explicit. However, compared with ABAQUS/Standard and ABAQUS/Explicit, NiftySim required much less computation time, i.e. in this example, 16 s for NiftySim (GPU version), 601 s for NiftySim (CPU version), 104 min for ABAQUS/Standard and 312 min for ABAQUS/Explicit.

### 3.2. Breast compression simulation

The breast compression in the plate compression experiments and the FE simulations was controlled by the applied displacement on the movable plate. Therefore, the breast shape change was determined only by the relative values of material model parameters of tissues. Here we chose fat as the reference material with an initial Young's modulus,  $E_f = 10$  kPa. The upper and lower limits of the three material parameters used in the optimization process were  $E$  (100 Pa–1 MPa),  $\nu$  (0.45–0.4999) and  $\eta$  (1 Pa–1 MPa).

Previous experimental observations suggested that the breast under plate compression exhibited an anisotropic deformation behaviour, with a reduced elongation in the anterior–posterior direction and an increased stretch in the inferior–superior direction (Tanner *et al* 2011). The anisotropic effect of breast tissues had been investigated with a linear, transversely isotropic, elastic model, and the plate compression was simulated by applying displacement constraints to the surface nodes of the breast. Here we explicitly modelled the interaction between the compression plates and breast tissues with a frictionless contact model and used nonlinear material models due to large strain. Figure 6 shows a comparison of breast shapes in MR images predicted using an isotropic NH hyperelastic model and a transversely isotropic

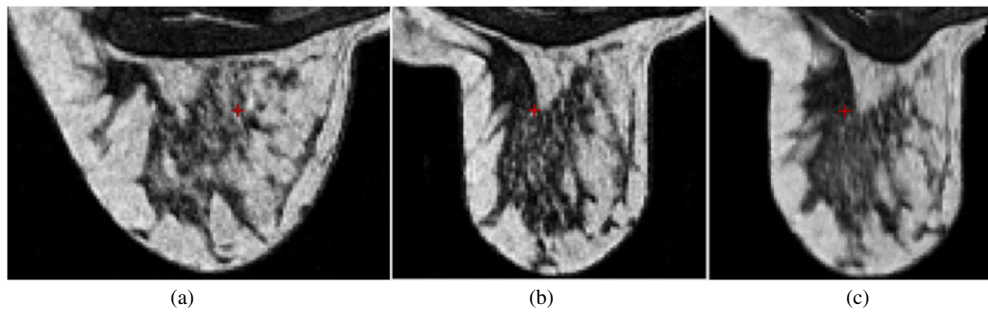


**Figure 7.** Example of central, axial ( $X$ - $Z$ ) slice images of a breast before and after medio-lateral compression (case 2): (a) the original undeformed MR image, (b) the original deformed MR image and (c) the FE-predicted MR image with a transversely isotropic heterogeneous model.

**Table 2.** Euclidean distance errors of 17 landmarks with four different material models.

Patient no	Landmark displacement (mm)	Euclidean distance error (mm)			
		Anisotropic heterogeneous model	Anisotropic homogeneous model	Isotropic heterogeneous model	Isotropic homogeneous model
Case 1	$27.62 \pm 8.16$	$5.85 \pm 2.80$	$8.52 \pm 2.90$	$10.34 \pm 3.20$	$19.54 \pm 3.68$
Case 2	$16.58 \pm 3.86$	$3.85 \pm 1.85$	$5.95 \pm 2.73$	$5.18 \pm 2.19$	$8.36 \pm 3.75$
Case 3	$23.29 \pm 6.41$	$5.68 \pm 2.95$	$6.02 \pm 3.15$	$6.60 \pm 3.27$	$13.53 \pm 3.89$
Case 4	$42.12 \pm 8.53$	$9.54 \pm 3.88$	$11.12 \pm 4.23$	$11.54 \pm 4.31$	$20.38 \pm 6.75$
Case 5	$13.92 \pm 2.66$	$3.18 \pm 1.69$	$3.95 \pm 1.58$	$3.56 \pm 1.75$	$5.12 \pm 1.93$

NH hyperelastic model. The solid lines denote the boundaries of a breast in the original MR images, and the dashed lines represent the boundaries of a breast in FE-predicted MR images. As shown in figure 6(a), the maximum size of the breast in the  $x$ -direction has almost no change after compression, and the stretch in the  $y$ -direction dominates the breast deformation, showing an anisotropic behaviour. Figure 6(b) clearly shows that the isotropic NH hyperelastic model is insufficient to predict the breast shape change, and figure 6(c) indicates that the transversely isotropic NH hyperelastic model with a simultaneous material parameter optimization can accurately capture the breast shape change under plate compression.

In the FE analyses, four kinds of material models were considered: (a) an isotropic homogeneous model, in which the breast was composed of one homogeneous material and modelled with an isotropic NH hyperelastic model; (b) an isotropic heterogeneous model, with the breast composed of different tissues and modelled with an isotropic, NH hyperelastic model; (c) an anisotropic homogeneous model, with the breast composed of one homogeneous material and modelled with a transversely isotropic, NH hyperelastic model; and finally (d) an anisotropic heterogeneous model, in which the breast was composed of different tissues and modelled with an anisotropic NH hyperelastic model. Figure 7 shows an example of an FE-predicted MR image with the transversely isotropic, heterogeneous material model (case 2). The prediction performance of the proposed approach was evaluated by calculating the Euclidean distance errors of 17 landmarks. The results are listed in table 2. From the change in the mean errors, we find that the prediction accuracy of FE analyses can be significantly improved when the breast is treated as a heterogeneous material or considered as an anisotropic material. The anisotropic, heterogeneous material model gives the best

**Table 3.** Optimized material model parameters.

Patient no	Tissue type	Anisotropic heterogeneous model			Isotropic heterogeneous model	
		$E/E_f$	$\nu$	$\eta/E$	$E/E_f$	$\nu$
Case 1	Fat	1.00	0.4983	23.63	1.00	0.4982
	Glandular	65.92	0.4982	27.25	33.77	0.4648
	Muscle	66.80	0.4517	61.97	19.55	0.4561
Case 2	Tumour	98.60	0.4988	40.25	71.93	0.4531
	Fat	1.00	0.4773	3.48	1.00	0.4531
	Glandular	0.55	0.4955	4.74	0.46	0.4775
Case 3	Muscle	97.22	0.4782	4.13	30.70	0.4515
	Fat	1.00	0.4950	4.16	1.00	0.4852
	Glandular	3.89	0.4763	4.22	0.22	0.4536
Case 4	Muscle	13.39	0.4760	0.034	1.21	0.4902
	Fat	1.00	0.4963	11.26	1.00	0.4502
	Glandular	2.97	0.4998	39.21	43.64	0.4768
Case 5	Muscle	28.65	0.4758	13.06	40.90	0.4643
	Fat	1.00	0.4509	3.39	1.00	0.4715
	Glandular	4.23	0.4980	0.018	5.58	0.4716
	Muscle	7.62	0.4990	3.27	49.02	0.4501

deformation estimation. Excepting case 4, the best mean errors for all four cases range from 3.18 to 5.85 mm, equivalent to an accuracy of between 1.1 and 2.0 voxels relative to the diagonal of a voxel ( $1.0 \times 1.0 \times 2.5 \text{ mm}^3$ ). Considering that we always have to make necessary simplifications and assumptions in FE simulations due to the uncertainties, e.g. the breast deformation due to patient movement, boundary constraints between pectoral muscle and chest wall and the positions of compression plates, the proposed method provides reasonable deformation predictions for all the cases. Table 3 lists the optimized material parameters for each tissue, for the anisotropic heterogeneous and isotropic heterogeneous models. A tendency of much stiffer muscle and stiffer tumour can be observed. For most cases, glandular tissue is stiffer than fat. However, in case 2, Young's modulus obtained for glandular tissue is smaller than that for fat. This could be explained by the fact that the fat tissue in the model is a mixture of fatty tissue, skin and Cooper's ligaments, and it can be strengthened by the skin and Cooper's ligaments, leading to a higher stiffness than that of glandular tissue.

#### 4. Discussion and conclusion

In this study, we proposed a patient-specific FE modelling framework for large breast deformation prediction, supported by a fast, GPU-based, dynamical explicit nonlinear FE solver. To minimize manual intervention and reduce the total time for patient-specific modelling, we implemented a semi-automatic method for tissue classification and a fully automated method for mesh generation. To avoid the difficulty in determining material property parameters of soft tissues *in vivo* for FE analyses, we presented a novel FE simulation approach with a simultaneous material parameter optimization for breast tissues.

The proposed method was tested by simulating and analysing the deformation of breasts under medio-lateral plate compression in five experiments, indented to approximate the compression occurring during x-ray mammography and MR-guided breast biopsy. Unlike previous studies, the interaction between breast tissues and compression plates was explicitly modelled and nonlinear, hyperelastic material models were used. To model the interaction between the breast tissues and the compression plates, we implemented a kinematic-type

contact algorithm in our GPU-based nonlinear finite element solver. It was evaluated by comparing the deformation fields of breasts calculated from both our solver and commercial FE package ABAQUS. Quasi-static simulation results showed that our solver provided essentially the same accuracy for deformation analyses as ABAQUS. However, our FE solver was much faster than ABAQUS. To support wider applications, the contact algorithm for modelling the interaction between two deformable objects has now been implemented in our FE solver. In the proposed method, the optimized FE prediction on breast deformation was obtained by maximizing the image similarity between the original deformed MR images and the FE-predicted MR images. However, alternative objective functions could be employed when a deformed MR image was not available. For example, for MRI to x-ray image registration, we could maximize the image similarity between a 2D real x-ray image and the pseudo 2D x-ray image obtained from the 2D projection of FE-predicted MR volume images (Mertzanidou *et al* 2010); in image-guided breast surgery, we could minimize the Euclidean error of fiducial markers on the breast surface (Carter *et al* 2006).

In the compression experiments used in this study, an anisotropic response to the deformation was observed for all the cases. This could be caused by the anisotropic nature of Cooper's ligaments and connective structures in the breast and the non-uniform initial deformation within the breast due to gravitational body force. Ideally, the deformation from gravitational force should be separated from the total deformation of tissues. Previous studies have attempted to remove the effect of the initial strain due to gravitation force. For example, a neutral buoyancy configuration of a breast was obtained by submerging the breast in water to offset the effect of gravity during MR imaging (Rajagopal *et al* 2008). Although the net buoyancy force could balance the overall weight of the breast with this method, the internal breast tissues will not be stress/strain free. This is due to the fact that buoyancy force is a surface force, while gravity is a body force acting throughout the whole volume of a breast. FE-based numerical methods were also proposed to estimate the zero-stress reference state of a breast from its deformed configuration under gravity loading by solving an inverse problem (Pathmanathan *et al* 2008, Rajagopal *et al* 2008). However, in these methods, the material parameters must be known in advance and the estimated undeformed breast shape at the zero-stress reference state was not validated because of difficulty in obtaining the reference state of breasts experimentally. Since soft tissues are always subjected to gravitational force and/or physical constraints in their natural state, the zero-strain state is not available. It is more convenient to consider the effect of initial strain/stress due to gravitational force as a part of material properties of soft tissues. In this study, the anisotropy of a breast was considered by using anisotropic material models or heterogeneous material models. In heterogeneous models, although each breast tissue is isotropic, the non-uniform spatial distribution of breast tissues will make a breast anisotropic. Numerical simulation results showed that the prediction accuracy on the displacement of landmarks could be significantly improved when breasts were treated as anisotropic materials. Further, a more accurate representation of the heterogeneity of breast tissues could be implemented by considering the partial volume effect. In the segmentation process of fat and fibroglandular tissue described in section 2.2.1, the probabilities of fibroglandular tissue and fat were calculated for each voxel; thus, it is possible to assign each voxel/element with different material parameters by using a suitable weighting scheme of material parameters between fibroglandular tissues and fat.

In this study, the skin was not explicitly included in the FE simulations; however, its reinforcement to fatty tissue and its effect on the anisotropic behaviour of the breasts have been implicitly considered by simulating fat as an anisotropic material. To construct more accurate biomechanical models, the skin should be segmented and explicitly simulated. Consequently, the interaction between the skin and breast tissue could be included, and a

frictional contact between the skin and the compression plate could also be considered. The effects of these interactions on breast deformation could be investigated under the proposed modelling framework with friction parameters (e.g. friction coefficient) as optimization variables. Experimentally determining friction characteristics between skin and plate should also be followed.

With the proposed method, the optimized material parameters for different tissues have been obtained for five cases. Through assessing more datasets and performing statistical analyses of material parameters, it may be possible to make the link between the material parameter values of each tissue, with age, the breast size, the breast density and its anatomical characteristics (e.g. volume ratio of fat). Subsequently, it could be used to provide guidance to assign reasonable material parameters for each tissue, in clinical applications, when the material parameter optimization is impossible due to limitations in time or resources.

The proposed method is suitable for large deformation prediction of breasts and has great potentials for wide applications such as multimodality image registration, image-guided surgery and surgical planning.

## Acknowledgments

The study is supported by the HAMAM project funded under the 7th Framework Program for Research, ICT-2007.5.3, and has been partially funded by EPSRC grant EP/E031579/1.

## References

- ABAQUS 2010 *ABAQUS Analysis User's Manual* (Providence, RI: Dassault Systèmes Simulia Corp.)
- Azar F S 2001 A deformable finite element model of the breast for predicting mechanical deformations under external perturbations *PhD Thesis* University of Pennsylvania
- Azar F S, Metaxas D N and Schnall M D 2001 A deformable finite element model of the breast for predicting mechanical deformations under external perturbations *Acad. Radiol.* **8** 965–75
- Azar F S, Metaxas D N and Schnall M D 2002 Methods for modeling and predicting mechanical deformations of the breast under external perturbations *Med. Image Anal.* **6** 1–27
- Bathe K J 1996 *Finite Element Procedures* (Englewood Cliffs, NJ: Prentice Hall)
- Bonet J and Burton A J 1998 A simple average nodal pressure tetrahedral element for incompressible and nearly incompressible dynamic explicit applications *Commun. Numer. Methods Eng.* **14** 437–49
- Cardoso M J, Clarkson M J, Ridgway G R, Modat M, Fox N and Ourselin S The Alzheimer's Disease Neuroimaging Initiative 2011 LoAd: a locally adaptive cortical segmentation algorithm *Neuroimage* **56** 1386–97
- Carter T, Tanner C, Crum W, Beechey-Newman N and Hawkes D J 2006 A framework for image-guided breast surgery *Medical Imaging and Augmented Reality (Lecture Notes in Computer Science vol 4091)* ed G-Z Yang, T Jiang, D Shen, L Gu and J Yang (Berlin: Springer) pp 203–10
- Chung J H, Rajagopal V, Nielsen P M E and Nash M P 2008 A biomechanical model of mammographic compressions *Biomech. Model. Mechanobiol.* **7** 43–52
- del Palomar A P, Calvo B, Herrero J, Lopez J and Doblare M 2008 A finite element model to accurately predict real deformations of the breast *Med. Eng. Phys.* **30** 1089–97
- Hallquist J O 2005 *LS-DYNA Theory Manual* (Livermore, CA: Livermore Software Technology Corporation)
- Han L H, Hipwell J, Mertzaniidou T, Carter T, Modat M, Ourselin S and Hawkes D J 2011 A hybrid FEM-based method for aligning prone and supine images for image guided breast surgery *IEEE Int. Symp. on Biomedical Imaging: From Nano to Macro* pp 1239–42
- Han L H, Hipwell J, Taylor Z, Tanner C, Ourselin S and Hawkes D J 2010 Fast deformation simulation of breasts using GPU-based dynamic explicit finite element method *Digital Mammography (Lecture Notes in Computer Science vol 6136)* ed J Martí, A Oliver, J Freixenet and R Martí (Berlin: Springer) pp 728–35
- Han L H, Noble J A and Burcher M 2002 A novel ultrasound indentation system for measuring biomechanical properties of *in vivo* soft tissue *Ultrasound Med. Biol.* **29** 813–23
- Joldes G R, Wittek A and Miller K 2009 Suite of finite element algorithms for accurate computation of soft tissue deformation for surgical simulation *Med. Image Anal.* **13** 912–9

- Kellner A L, Nelson T R, Cervino L I and Boone J M 2007 Simulation of mechanical compression of breast tissue *IEEE Trans. Biomed. Eng.* **54** 1885–91
- Krouskop T A, Wheeler T M, Kallel F, Garra B S and Hall T 1998 Elastic moduli of breast and prostate tissues under compression *Ultrasonic Imaging* **20** 260–74
- Lapuebla-Ferri A, del Palomar A P, Herrero J and Jiménez-Mocholí A-J 2011 A patient-specific FE-based methodology to simulate prosthesis insertion during an augmentation mammoplasty *Med. Eng. Phys.* **33** 1094–102
- Lorensen W E and Cline H E 1987 Marching cubes: a high resolution 3d surface construction algorithm *SIGGRAPH Comput. Graph.* **21** 163–9
- Mertzaniidou T, Hipwell J, Cardoso M, Tanner C, Ourselin S and Hawkes D J 2010 X-ray mammography—MRI registration using a volume-preserving affine transformation and an EM-MRF for breast tissue classification *Digital Mammography (Lecture Notes in Computer Science vol 6136)* ed J Martí, A Oliver, J Freixenet and R Martí (Berlin: Springer) pp 23–30
- Netter F H 2010 *Atlas of Human Anatomy* 5th edn (Philadelphia, PA: Saunders)
- Pathmanathan P 2006 Predicting tumour location by simulating the deformation of the breast using nonlinear elasticity and the finite element method *PhD Thesis* Oxford University
- Pathmanathan P, Gavaghan D J, Whiteley J P, Chapman S J and Brady J M 2008 Predicting tumor location by modeling the deformation of the breast *IEEE Trans. Biomed. Eng.* **55** 2471–80
- Rajagopal V, Chung J-H, Highnam R P, Warren R, Nielsen P M F and Nash M P 2010 Mapping microcalcifications between 2D mammograms and 3D MRI using a biomechanical model of the breast *Computational Biomechanics for Medicine* ed K Miller and P M F Nielsen (New York: Springer) pp 17–28
- Rajagopal V, Nash M, Highnam R and Nielsen P 2008 The breast biomechanics reference state for multi-modal image analysis *Digital Mammography (Lecture Notes in Computer Science vol 5116)* ed E Krupinski (Berlin: Springer) pp 385–92
- Ruiter N V, Stotzka R, Gemmeke H, Reichenbach J and Kaiser W 2002 Automatic image matching for breast cancer diagnostics by a 3d deformation of the mamma *Biomed. Tech.* **47** 644–7
- Ruiter N V, Stotzka R, Muller T O, Gemmeke H, Reichenbach J R and Kaiser W A 2006 Model-based registration of x-ray mammograms and MR images of the female breast *IEEE Trans. Nucl. Sci.* **53** 204–11
- Samani A and Plewes D 2004 A method to measure the hyperelastic parameters of *ex vivo* breast tissue samples *Phys. Med. Biol.* **49** 4395–405
- Samani A, Zubovits J and Plewes D 2007 Elastic moduli of normal and pathological human breast tissues: an inversion-technique-based investigation of 169 samples *Phys. Med. Biol.* **52** 1565–76
- Studholme C, Hill D L G and Hawkes D J 1999 An overlap invariant entropy measure of 3D medical image alignment *Pattern Recognit.* **32** 71–86
- Tanner C, Schnabel J A, Hill D L G, Hawkes D J, Leach M O and Hose D R 2006 Factors influencing the accuracy of biomechanical breast models *Med. Phys.* **33** 1758–69
- Tanner C, White M, Guarino S, Hall-Craggs M A, Douek M and Hawkes D J 2011 Large breast compressions: observations and evaluation of simulations *Med. Phys.* **38** 682–90
- Taylor Z A, Cheng M and Ourselin S 2008 High-speed nonlinear finite element analysis for surgical simulation using graphics processing units *IEEE Trans. Med. Imaging* **27** 650–63
- Taylor Z A, Comas O, Cheng M, Passenger J, Hawkes D J, Atkinson D and Ourselin S 2009 On modelling of anisotropic viscoelasticity for soft tissue simulation: numerical solution and GPU execution *Med. Image Anal.* **13** 234–44
- Tzu-Ching S, Chen J-H, Liu D, Nie K, Sun L, Lin M, Chang D, Nalcioğlu O and Su M-Y 2010 Computational simulation of breast compression based on segmented breast and fibroglandular tissues on magnetic resonance images *Phys. Med. Biol.* **55** 4153
- Van Houten E E W, Doyley M M, Kennedy F E, Weaver J B and Paulsen K D 2003 Initial *in vivo* experience with steady-state subzone-based MR elastography of the human breast *J. Magn. Reson. Imaging* **17** 72–85
- Wittek A, Joldes G, Couton M, Warfield S K and Miller K 2010 Patient-specific non-linear finite element modelling for predicting soft organ deformation in real-time: application to non-rigid neuroimage registration *Prog. Biophys. Mol. Biol.* **103** 292–303